Pore Scale Inertial Flow Simulations in 3-D Smooth and Rough Sphere Packs using Lattice Boltzmann Method

C. Chukwudozie
The Craft and Hawkins Dept. of Petroleum Engineering, Louisiana State University and A & M College, Baton Rouge, LA 70803

M. Tyagi
The Craft and Hawkins Dept. of Petroleum Engineering, Center for Computation and Technology (CCT), Louisiana State University and A & M College, Baton Rouge, LA 70803

DOI 10.1002/aic.14232
Published online October 25, 2013 in Wiley Online Library (wileyonlinelibrary.com)

Pore-scale inertial flows in periodic body centered cubic (BCC) arrays of smooth and rough sphere packs were simulated using lattice Boltzmann method. Computed velocity fields were visualized and averaged to calculate macroscopic flow parameters characteristic of porous media such as permeability, tortuosity, and β factor as well as the transition Reynolds number values and compared well with established correlations. Furthermore, hemispherical depositions on the smooth spheres in the regular BCC array were used to calculate roughness induced changes in macroscopic flow parameters. As the next step toward simulating inertia dominated flow in natural porous media, simulations were validated for low Reynolds number flow in a three-dimensional (3-D) CT image of irregular pack of uniform diameter spheres. This work aims to define 3-D canonical studies for roughness induced inertial flows in porous media and to assess the capability of LBM for simultaneous prediction of absolute permeability and β factor. © 2013 American Institute of Chemical Engineers *AIChE J*, 59: 4858–4870, 2013

Keywords: inertial flow, porous media, Darcy-Forchheimer equation, beta factor, lattice Boltzmann method

Introduction

Accurate prediction of the macroscopic flow parameters needed to describe flow in porous media requires good knowledge of flow field distribution in the pore spaces. Porous media flow spans many orders of spatial-temporal scales and for each scale, different forms of flow governing equations are applicable and have been used to model fluid flow.[1] At the pore-scale level (typically μm), Navier-Stokes (NS) equations as well as lattice Boltzmann method (LBM) with appropriate equilibrium distribution function are representative physical models governing fluid motion. Furthermore, the empirical relationships like Darcy and Forchheimer equations at the macroscale (typically cm to m) description of porous media can also be derived from the classical Navier-Stokes (NS) equations under certain assumptions.[2–4] For use of the empirical relations, it is important to understand flow distribution at the pore scale and its contribution to the values of the macroscopic flow parameters like permeability, tortuosity and the beta factor that are important components of the empirical equations. Traditionally, these parameters are obtained from experiments while analytical expressions also exist that relate these macroscopic properties to some flow/geometry attributes of the porous media.[1] While the analytical expressions are only good approximations for simple cases and may not be applicable in a wide range of media, experimental determination of these parameters can be rather time-consuming and expensive. In addition, these experiments do not directly capture the effect of pore geometry on the flow distribution, and, thus, on the predicted value of these parameters. To circumvent these problems, numerical methods based on the discretization of the Stokes and Navier-Stokes equations are employed to solve the flow problems at pore-scale level than those to which the Darcy and non-Darcy equations are applied. Results of these simulations are averaged over the whole simulation domain to obtain the macroscopic flow parameters. Earlier numerical studies for beta factor prediction also involved either less detailed models such as pore-network model[5] or stochastically generated 2-D pore spaces.[6] However, with advances in microtomography technology and its application in digital imaging of real rocks, these methods have been applied to simulate flow in real and complex porous media as found in petroleum reservoirs. Modeling the high-flow rates encountered in the near wellbore region of high-permeability reservoirs requires knowledge of the Forchheimer coefficient (referred to as beta factor). Experimental determination of the coefficient requires relatively large (1.5 × 2 inch) rock samples using careful procedures and interpretations. On the other hand, the physical volume for LBM computations are typically about 1 mm^3 and can be obtained from drill cuttings and other sources without resorting to core plugs (which can be prohibitively expensive for deepwater reservoirs). However, upscaling of pore-scale flow details and

Correspondence concerning this article should be addressed to M. Tyagi at mtyagi@lsu.edu.

deduced parameters from mm^3 scale to large-scale heterogeneous porous media still remains an open problem. Although the size of the volume required for LBM computations makes it difficult to reflect the heterogeneity inherent in natural porous media as encountered in petroleum reservoirs, nonetheless, the outlined approach allows accurate determination of the coefficient at the scale of the samples (few mm^3). In this article, one such case of porous media used for simulation is a computational domain consisting of irregular distribution of spherical particles of uniform grain diameter generated by computed tomography (CT) imaging.

Finite difference approximations (FDM), finite volume (FVM), and various forms of the finite element methods (FEM) are traditional numerical discretization schemes for NS equations that have long been used to solve flow problems in discretized porous media.[7] Recently, the LBM has also been applied to simulate compressible and incompressible flow.[8,9] The use of these numerical methods in estimating flow in porous media requires an accurate model of the 3-D porous structure and the discretization of the model into pore and solid phases, so that the flow equations can be solved in the pore spaces with the appropriate boundary conditions applied at the pore and solid interfaces.[10] In real porous media, the pore boundaries are arbitrarily complex and make it difficult to specify boundary values and solve the problem using the FDM, FVM, and FEM that require unstructured or block structured meshes to represent complex pathways. Unlike the conventional computational fluid dynamics (CFD) methods based on the macroscopic continuum equations, the LBM uses a mesoscopic equation (pore-scale level), specifically the Boltzmann equation to determine macroscopic fluid dynamics. It has the advantage of being flexible in the specification of variables on the complex boundaries in terms of simple particle bounce back and reflection. This flexibility has opened up the potential in its use for modeling and simulating flow in complex media like porous rocks.[10] Since its algorithm is based on the nearest neighbors, it is also amenable to parallel computing and has taken advantage of the substantial increase in computing capabilities over the years. Chen and Doolen[8] and Aidun and Clausen[9] have reviewed development of the method and its application to various areas like single and multiphase flows, deformable particles and fiber suspensions. The earliest reported applications of the LBM in porous media simulation are by Succi et al.[11] They used this method to estimate the permeability of 3-D porous medium and obtained values that were comparable to the Kozeny equation. Thereafter, Ferreol and Rothman[12] and Martys and Chen[13] simulated single- and two-phase flow in porous media using LBM. Recently, Jin et al.[14] built virtual samples of consolidated and unconsolidated reservoir rocks by applying the physics based reconstruction approach and directly calculated the absolute permeability of the medium using results obtained from the LBM simulation of flow in the domain. Others studies like Sholokhova et al.[15], Nabovati and Sousa[16] and Rahmati and Ashrafizaadeh[17] also applied the method for single phase flow while Pan et al.[18] simulated two-phase flow. Kang et al.[19] presented a review of LBM in the reactive flows through porous media.

Among several other LBM studies relevant to this work, a few studies[20–22] are also noted without being an exhaustive review. Jin et al.[14] studied the relationship between permeability and irreducible water saturation, represented by the amount of clay deposited on the solid phase of the porous medium. Using the LBM on a synthetic generated 3-D image of the pore-space domain, the permeability was estimated for different morphology of dispersed clay in the medium. The results of these numerous efforts compared well with appropriate analytical and experimental data. However, most of the works treated the permeability as a single scalar quantity and in cases where it was considered to be a tensor, the principal directions were decided *a priori* as the direction of the components of the pressure gradients and only the diagonal components were estimated.

In this study, we apply the LBM to simulate flow in computer generated and CT-imaged 3-D porous media of a sphere pack. An open source code, the OpenLB (www.openlb.org) is used to implement the algorithm. Flow is simulated beyond the regime of linear relationship (Darcy's law) between the pressure gradient and the volume averaged velocity field. The results are then arranged in the form of the Darcy and Forchheimer equations to obtain flow permeability and non-Darcy coefficient. Thereafter, flow distributions in the porous media are visualized while corresponding streamlines through the connected pore spaces are highlighted. One research objective is to evaluate and establish LBM as a credible tool for computing inertial flow parameter in simple 3-D canonical cases of porous media. To that end, LBM simulations systematically build on regular sphere packs, regular but rough sphere packs and lastly, an irregularly arranged CT-imaged sphere pack. Recently, many commercial companies have promoted LBM as a potential tool for digital rocks with limited validation against experiments (almost invariably in Darcy regime). Johns et al.[23] used magnetic resonance imaging (MRI) to study the flow transition from creeping flows to inertial flows in isolated pores of sphere packs. Suekane et al.[24] used MRI technique to observe jet like flow in the center of pores with eddy structures in the stagnant spaces in plane perpendicular to main flow direction at much higher flow rates. Gunjal et al.[25] simulated the inertial flows in packed beds using unstructured finite volume CFD solver (commercial code, Fluent™), and compared against the experimental data of Suekane et al.[24] to show a good agreement between the computational results with the data. Robbins et al.[26] validated single-phase CFD model against the MRI data for inertial flows in packed bed reactors. CFD code was based on unstructured finite volume discretization of compressible Navier-Stokes equations. To authors' knowledge, the capability of LBM for simultaneous prediction of absolute permeability and beta factor has not been verified and validated in any systematic study in the open literature, and, thus, it is one of the original attempts to define 3-D canonical studies for inertial flows in porous media.

Empirical relationships for inertial flow in porous media

Darcy's law given by Eq. 1 is commonly used to model flow in porous media

$$\langle \vec{u} \rangle = -(K \nabla p)/\mu \tag{1}$$

This regime is characterized by very low Reynolds number (Eq. 2) since fluid flow is dominated by the viscous forces such that the pressure gradient responsible for the flow is linearly proportional to the superficial velocity

$$Re = \rho u D_p/\mu \tag{2}$$

D_p, μ, ρ, and u are characteristic particle dimensions, fluid viscosity, density and velocity magnitude, respectively.

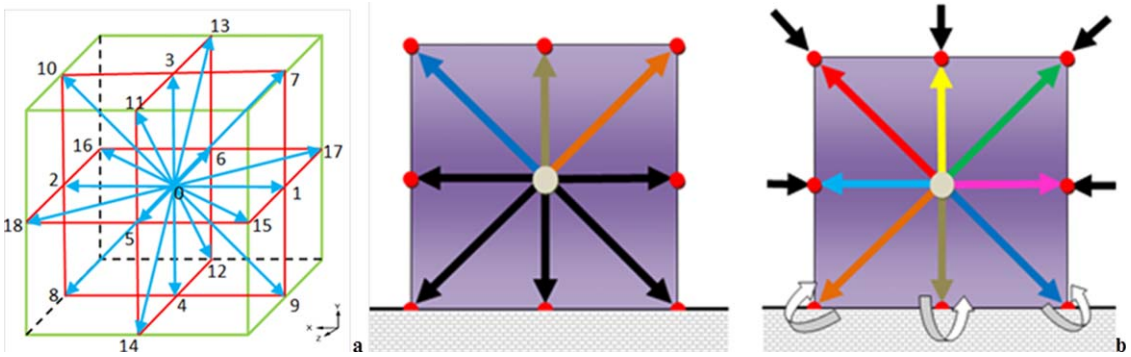

Figure 1. Lattice Boltzmann model details.

(a) Schematic of D3Q19 lattice directions, and (b) schematic of particle bounce back scheme to enforce no-slip on solid surfaces. [Color figure can be viewed in the online issue, which is available at wileyonlinelibrary.com.]

Permeability tensor (K) is a macroscopic medium property that acts on the pressure gradient and transforms it into a velocity vector (Eq. 1). This property is highly dependent on the size, distribution, and connectivity of the pore spaces. It defines a physical relationship between the porous media, the fluid flowing through it, and the conditions imposed to obtain this flow process. Thus, a quantitative and qualitative prediction of this property in porous media requires an accurate microscopic model of the porous media and an understanding of the contribution of the microstructure of the medium to flow distribution.

The simplest microscale approach to predict permeability while accounting for the pore geometry are the Ergun and Kozeny-Carman equations, respectively, using the Hagen-Poiseuille equation for flow and pressure drop relationship in a conduit

$$k_{Ergun}=\frac{\varphi^3 D_p^2}{A_p(1-\varphi)^2};\ k_{CK}=\frac{\varphi^3 D_{p2}^2}{A_p\tau(1-\varphi)^2} \tag{3}$$

k is permeability, D_{p2} is an equivalent sphere diameter, and Φ is porosity. $A_p=180$ and 150 for Kozeny-Carman and Ergun equations, respectively.[1] In addition, medium tortuosity (τ) is a stream-wise length measure of the irregularity of the pore spaces. It is normally a tensor and its components are defined as the square of the ratio of the actual distance traveled by the fluid particles to the length of the media, in the direction of the applied pressure gradient

$$\tau=\left(\frac{L_i}{L}\right)^2 \tag{4}$$

L and L_i are the length of the media and the actual distance traveled by the fluid particles in the porous media, respectively. Readers are cautioned about the correct interpretation of tortuosity as "hydraulic tortuosity" in this article as the meaning of tortuosity is different when used by physicists, engineers, or geologists to describe different transport process using geometrical, electrical, diffusional, or hydraulic tortuosity values.[27]

Under high-flow rate conditions, inertial forces become large and the linear relationship between pressure gradient and velocity does not hold. Several criteria have been proposed to identify the threshold beyond which the linear relationship fails. The Reynolds number based on particle diameter (Eq. 2) is widely used for sphere packs and critical values between 1 and 10 obtained from experiments and numerical simulations have been reported in literature. In addition, several attempts have been made to model this nonlinear relationship using the Forchheimer equation (Eq. 5)

$$-\nabla p=\mu K^{-1}\langle\vec{u}\rangle+\rho\beta|\langle\vec{u}\rangle|\langle\vec{u}\rangle \tag{5}$$

β is referred to as the beta factor (non-Darcy coefficient) that quantifies the amount of inertial contribution to the total pressure drop. In this region, the apparent permeability is not constant but varies with flow velocity and is modeled using the non-Darcy coefficient. Like intrinsic permeability, β is also a tensor quantity. It is assumed to be a constant in the range of the Forchheimer regime and is considered to be a property of the porous medium like permeability, tortuosity, and porosity.[28,29] A number of empirical and analytical expressions have been proposed to estimate the beta factor with the simplest being the Ergun equation modeled for collection of spheres and for cylindrical conduits using the bundle of tube model and from which the permeability can also be obtained. According to Dullien[1], the non-Darcy coefficient and permeability are proportional to the particle/conduit diameter and medium porosity as given

$$\beta=\frac{1.75(1-\varphi)}{\varphi^3 D_p} \tag{6}$$

Even the Forchheimer equation remains subject to numerous criticisms as several authors[30] have doubted the ability of the quadratic term in this relationship to capture all flow regimes beyond the Darcy flow (viscosity dominated). It is not the aim of this article to further put the numerous empirical relations to test, but to use the Darcy and Forchheimer equations as functional relationships for analysis of the LBM simulation results to calculate the permeability and the non-Darcy coefficient. LBM simulation results are averaged over the whole simulation domain to calculate porosity, permeability, tortuosity, and non-Darcy coefficient and arranged in the form of the empirical relations to obtain the flow parameters.

Overview of Lattice Boltzmann Method (LBM)

LBM is an established numerical scheme[10] for simulating fluid flow problems in terms of a single variable, the particle distribution function, compared to the traditional CFD methods that solve the Navier-Stokes equation for the macroscopic variables of pressure and velocity. The numerical scheme is derived from microscopic physics as it considers fluids to consist of many tiny flow particles. The collective behavior of many of these tiny flow particles results in the macroscopic dynamics of the fluid. Even though the method is derived from the microscopic physics, it is still able to recover accurately the solutions of Navier-Stokes equations in the hydrodynamic limit of low Mach number. The desired

macroscopic variables can be recovered as moments of the distribution function. LBM has several advantages in pore-scale modeling because of the flexibility in treating complex boundary conditions using bounce back schemes at appropriate spatial locations flagged as wall sites.

The lattice Boltzmann equation (LBE) is a discrete form of the continuous Boltzmann equation where time and space coordinates are discretized with velocity range in phase space limited to a finite set of vectors that represent the directions in which the fluid particles can travel. For this study, the D3Q19 model is used (Figure 1a)

$$\frac{\partial f_\alpha}{\partial t}+\vec{e}_\alpha\cdot\nabla f_\alpha=\Omega \tag{7}$$

$f_\alpha(\vec{x},\vec{e}_\alpha,t)$ is the fraction of fluid particles that have traveled in any of the 19 directions represented by α. Particle interactions are achieved by discretizing and solving a microscopic kinetic equation for the particle distribution function $f_\alpha(\vec{x},\vec{e}_\alpha,t)$ in each time step. D3Q19 has 18 discrete lattice velocities with one fluid particle at rest. Of the 18 directions, 6 are to the nearest neighbors while 12 are in the diagonal directions

$$\vec{e}_\alpha=\begin{cases}(0,0,0);\ \alpha=0\\ (\pm1,0,0),(0,\pm1,0),(0,0,\pm1);\ \alpha=1,2,3,4,5,6\\ (\pm1,\pm1,0),(\pm1,0,\pm1),(0,\pm1,\pm1);\ \alpha=7,8,9,10,11,12,13,14,15,16,17,18\end{cases}$$

Algorithm

The basic LBM algorithm consists of two steps; Particle streaming and collision.

1. Streaming: This step involves the transfer of the particle distribution function value between nodes along a particular velocity direction as shown below

$$f_\alpha(\vec{x}+\vec{e}_\alpha dt,\vec{e}_\alpha,t+dt)=f_\alpha^*(\vec{x},\vec{e}_\alpha,t) \tag{8}$$

1. Collision: During collision step momentum exchange between the particles take place due to collision with each other in a particular node as shown below

$$f_\alpha^*(\vec{x},\vec{e}_\alpha dt)=f_\alpha(\vec{x},\vec{e}_\alpha dt)+\Omega \tag{9}$$

$f_\alpha^*(\vec{x},\vec{e}_\alpha dt)$ is the post collision distribution function, $f_\alpha(\vec{x},\vec{e}_\alpha dt)$ is the precollision distribution function, and Ω is the collision operator. The collision operator accounts for the fact that after collision, the total number of particles in a node along a particular direction changes. This is because of the momentum exchange between the particles after collision. These two steps are combined with appropriate internal and external boundary conditions to simulate flow in the whole domain.

Kinetic model

The Bhatnagar-Gross-Krook (BGK) model approximates collisions to relax toward an equilibrium distribution function defined by the macroscopic velocity at that particular point. From an initial state, the particle distribution functions evolve at each time step over the whole simulation domain according to the BGK kinetic equation. The collision term in the BGK model is given by

$$\Omega=-\frac{1}{\lambda}\left[f_\alpha(\vec{x},\vec{e}_\alpha dt)-f_\alpha^{eq}(\vec{x},\vec{e}_\alpha dt)\right] \tag{10}$$

$f_\alpha^{eq}(\vec{x},\vec{e}_\alpha dt)$ is the equilibrium distribution function which is obtained from the macroscopic values of the velocity and density as given as following

$$f_\alpha^{eq}(\vec{x},t)=w_\alpha\rho(\vec{x},t)\left[1+3\vec{e}_\alpha\cdot\vec{u}+9\frac{(\vec{e}_\alpha\cdot\vec{u})^2}{2}-\frac{3|\vec{u}|^2}{2}\right] \tag{11}$$

w_α is the weight factor for the α velocity direction while ρ and u are the macroscopic density and velocity, respectively, all in lattice units. In Eq. 10, λ is the dimensionless relaxation time parameter and it measures the rate at which the distribution functions tend toward equilibrium value and controls the viscosity of the fluid as following

$$v_{lu}=\frac{(2\lambda-1)}{6}\text{ where }\lambda>0.5 \tag{12}$$

Recently, the use of multi-relaxation time (MRT) approach over a single scalar value of λ has been advocated for its ability to better model flows in porous media. However, the aim of this manuscript is not to compare different closure models for collision operator.

Body forces and inflow/outflow boundary conditions

A pressure gradient is imposed on the fluid in the domain by using a uniform body force added at each time step to the fluid particles in the pore space. The body force produces the same amount of flow as the pressure driven flow since its value is calculated from the pressure gradient. The particles are accelerated at each time step by addition of this force to the distribution functions in the direction of the imposed pressure gradient while a corresponding amount of the body force is subtracted from particles moving in the opposite direction.[31,32]

Pressure driven flow will be simulated in the porous media described previously to obtain the flow properties. One of two approaches will be used to impose the pressure gradient on the porous media and for each, pressure gradient in lattice units is related to that in physical units by Eq. 13

$$\left(\frac{dp}{dx}\right)_{p_i}=\rho_p\frac{\Delta x}{\Delta t^2}\left(\frac{dp}{dx}\right)_{lu_i} \tag{13}$$

The first method is the body force approach used on the periodic domains; the smooth and rough BCC domains, respectively, while the second is the density difference approach for the disordered sphere pack. In the body force approach, pressure gradient is imposed on the fluid in the domain by using a uniform body force (b_{fi}) added at each time step to the fluid particles in the pore space. The body force produces the same amount of flow as the pressure driven flow since its value is calculated from the pressure gradient

$$\left(\frac{dp}{dx}\right)_{lu_i} = b_{f_i} \tag{14}$$

For density difference approach, pressure gradient to drive flow in the porous media is implemented by imposing fluid density gradient in the direction of flow by using Eq. 15

$$\left(\frac{dp}{dx}\right)_{lu_i} = \frac{\Delta\rho_{lu}}{3N_i} = \frac{\rho_{inlet} - \rho_{outlet}}{3N_i} \tag{15}$$

Initial and no-slip boundary conditions

Initial conditions of a system are only important for time-dependent flows. However, to calculate the porous media flow parameters, the final steady state for a particular body force is desired and it should be independent of the initial conditions. Thus, to speed up the simulation, an initial velocity distribution of 0.01 Lu was defined over the whole domain.

No-slip boundary condition at the fluid/solid interface is implemented using the standard bounce back scheme shown in Figure 1b. In this scheme, the distribution function from a fluid node to a neighboring solid node is bounced back along the same link. This ensures a zero velocity vector on the bounce back node. In addition, since the domains are periodic, periodic boundary condition will be used on all the external faces such that the distribution function leaving a particular boundary face re-enters the domain on the opposite boundary, along the same link.[33]

Lattice units

In LBM, parameterized values of the lattice constants and fluid in lattice units are used in simulation while correspondence between the real physical system being simulated and the parameterized simulation is achieved through Reynolds number (principle of dimensional similarity). Important lattice constants used for relating measurements in the two unit systems are; resolution, discrete time step and viscosity in lattice units

$$\Delta x = \frac{1}{N_i}; u_p = u_{lu}\frac{\Delta x}{\Delta t}; v_p = v_{lu}\frac{\Delta x^2}{\Delta t}; p_p = p_{lu}\rho_p\frac{\Delta x^2}{\Delta t^2} \tag{16}$$

Δx is resolution, Δt is the time step, N_i is the number of voxels in reference direction, u is the velocity, v is the kinematic viscosity, ρ is the fluid density, and p is the pressure.

Calculation of Macroscopic Flow Parameters

Tortuosity. The tortuosity which is a lineal measure of the complex pathways in the pore spaces is estimated using the following two equations

$$\tau = \left(\frac{\sum u_{mag}}{\sum |u_j|}\right)^2 \tag{17}$$

$$\tau_1 = \left(\frac{\sum u_{mag}}{\sum u_j}\right)^2 \tag{18}$$

It is expected that τ_1 will be greater than τ since it considers negative values of velocities that arise due to recirculation at high-flow conditions. Readers are cautioned about the correct interpretation of tortuosity as "hydraulic tortuosity" in this article because different meanings of tortuosity are used by different domain researchers to describe corresponding transport process using geometrical, electrical, diffusional, or hydraulic tortuosity values.[27]

Permeability. The permeability is calculated from lattice unit values of the flow, fluid and domain properties using

$$k_{ij} = \frac{\Delta x^2 v_{lu} u_{lui}}{(dp/dx)_{luj}} \tag{19}$$

Beta factor. The beta factor is obtained as the slope of the plot of the inverse of the apparent permeability vs. the pseudo-Reynolds number (not a dimensionless number, unit 1/m) as presented in the Eq. 20, where the intercept on the inverse apparent permeability axis provides an estimate of the intrinsic permeability of the medium

$$\frac{1}{k_{app}} = \frac{\nabla p}{\mu\langle u\rangle} = \frac{1}{k_{\text{int}}} + \beta\frac{\rho\langle u\rangle}{\mu}; \qquad \text{Re}_{ps} = \frac{\rho\langle u\rangle}{\mu} \tag{20}$$

Performance of OpenLB Code

To execute the LBM algorithm, we used an open source code known as OpenLB[34] (www.openlb.org). It is a numerical framework for lattice Boltzmann simulations that runs both in series and in parallel using either MPI or OpenMP. OpenLB scales well over thousands of cores, even with small lattices. During each iteration, the code implements collision and propagation of the distribution function. Using this package, it is easy to reach regimes in which billions of lattice sites are processed in 1 s. Thus, code performance is measured in lattice updates per second and it represents the number of lattice sites that complete a collision and propagation cycle in 1 s. Units are Sus, Mega-sus (Msus), Giga-sus (Gsus).

The performance of the OpenLB code used for our simulation was tested by running on a number of cores on the high performance computing (HPC) resources at Louisiana State University (LSU) and noting the wall time it took to execute a fixed number of iterations. I/O operations were reduced to minimize the time spent by the processors in writing out image and data files. Strong scaling results and efficiency of the OpenLB code for the 250^3 random sphere pack computational domain, on the HPC systems are shown in Figure 2. Figure 2a shows a significant decrease in execution time as more cores are used in running the code. Beyond 56–64 cores, the benefit of using more processors for simulating flow on the 250^3 computational domain diminishes as significant time was not gained by running on more nodes. This is supported by the curve tending toward an asymptotic value at higher processor counts. Efficiency measures the speed of code execution with increasing number of cores, and for an ideal system (i.e., 100% efficiency), a linear relationship should be maintained between execution speed and number of cores. In Figure 2b, the code performance deviates from the initial linear relationship, as more nodes are added to the communication domain. Beyond the linear regime, the speed of execution does not scale up with the increasing number of processors and this corresponds to the diminishing execution speed observed in Figure 2a.

Numerical Results

Poiseuille flow in a pipe

In selecting a relaxation time that provides accurate results for the porous media simulation in this work, we solve for

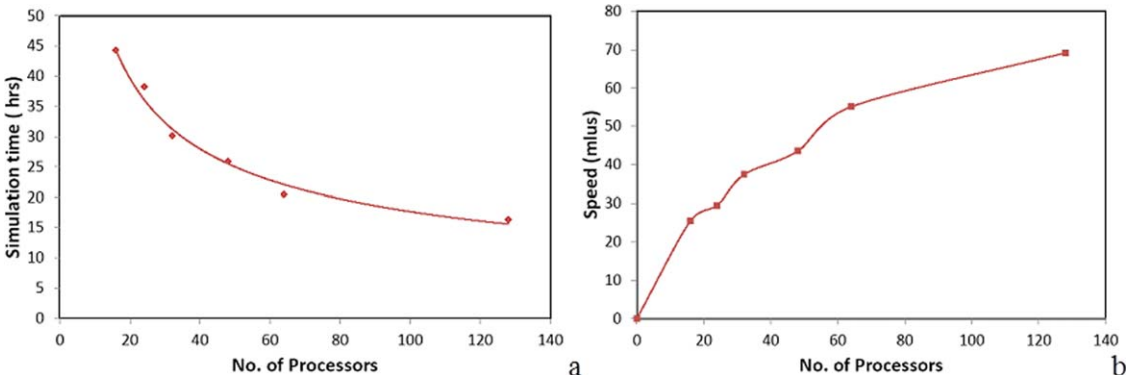

Figure 2. Parallel code performance.

(a) Strong scaling of OpenLB over multiple processors, and (b) efficiency of OpenLB. [Color figure can be viewed in the online issue, which is available at wileyonlinelibrary.com.]

flow in a uniform diameter pipe using different relaxation times and comparing the results with the theoretical Poiseuille flow equation given below

$$\vec{u}_p = -\frac{(R^2 - r^2)}{4\mu}\nabla p \tag{21}$$

The cylindrical pipe of dia. 175 μm is inserted in a square domain of 100^3 computational size. Thus, diameter of the pipe which is less than the length of the side of the square domain is 92 *lu*. Varying the relaxation time from 0.7–1.3, the simulated velocity profile shown in Figure 3a, including that obtained from Eq. 21, on a line through the center of the pipe is plotted for flow driven by a pressure gradient of 1×10^4 N/m^2. The plots are very close to the theoretical solution and estimating the average deviation error from Eq. 22, it is seen that the error decreased as the relaxation time increased as shown in Table 1. However, relaxation time $\lambda = 0.9$ will be used for further simulations as it has been reported to be optimum for porous media simulation. In addition, it allows for higher Re flows compared to when larger relaxation times are used. Flow distribution in the pipe is shown in Figure 3b and the maximum velocity is clearly seen to be at the pipe center

$$Error = \frac{1}{46}\sum \left| \frac{u_{\lambda_i} - u_{p_i}}{u_{p_{\max}}} \right| \times 100 \tag{22}$$

u_{λ_i} is the velocity at node i obtained from LBM simulation using relaxation time λ, is the velocity obtained from Poiseuille equation (Eq. 21) while $u_{p_{\max}}$ is the maximum velocity at the center of the pipe using the Poiseuille equation. The bundle of tube method gives the permeability of a circular pipe of radius R as $k = 0.125R^2$. With the dimensions of the simulated pipe, this gives a permeability of 970 D. This value shows good comparison with the simulation estimates which varied between 957–946 D for $\lambda = 0.7$–1.3.

Body centered cubic (BCC) sphere pack

A porous medium consists of grains (solid matrix) and pore spaces (voids). In this context, porous medium is a multicomponent material. Its domain can be discretized so that the distribution of the position vector of the nodes is described by value 1 in the voids and 0 inside the grains. The first porous media to be studied is shown in Figure 4a. It consists of a uniform distribution of smooth spheres in a body centered cubic arrangement. The length of the cube is 175 μm.

Single-phase fluid flow was simulated in this medium until steady state was reached. Using Eqs. 17 and 18, two estimates of the average tortuosity were calculated at different Re while the components of the permeability tensor were obtained from the simulation results using Eq. 19, at low values of average velocity for which Darcy's law is valid. Since the domain geometry is periodic with respect to its boundaries, the diagonal components of the tortuosity, permeability and beta factor, respectively for the BCC sphere pack will be the same while the off-diagonal components will be zero.

Next, we quantified the effect of lattice resolution on our simulation by varying the size of the computational domain for the regular BCC distribution of spheres and calculating the permeability from the simulation results. 400^3, 350^3, 300^3, 200^3, 100^3, and 50^3 computational grid sizes were

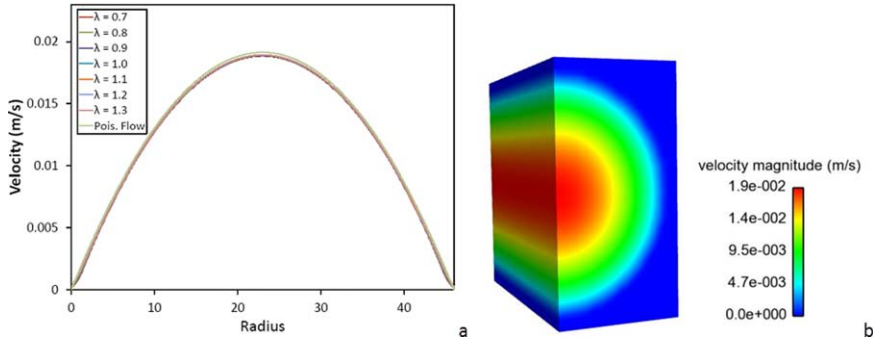

Figure 3. Poiseuille flow in pipe.

(a) Parabolic velocity profile, and (b) section through laminar flow field in a pipe. [Color figure can be viewed in the online issue, which is available at wileyonlinelibrary.com.]

Table 1. Effect of Relaxation Time Parameter on the Mean Error between Computed Results and Theoretical Poiseuille Flow Profile.

λ	0.7	0.8	0.9	1.0	1.1	1.2	1.3
Error (%)	1.53	1.53	1.42	1.33	1.26	1.19	1.13

used, respectively and the permeability estimates were observed to change slightly with increasing resolution, as shown in Figure 5. The change in permeability was insignificant with a difference of about 0.143% obtained between the values at resolutions corresponding to 400^3 and 50^3 computational grids, respectively. At this computational grid sizes, the image resolution levels were deemed adequate to resolve the pore spaces and produce reliable LBM simulation results. To simulate high Re flows and reduce computational times, 350^3 lattice size is used for further simulations. In addition to resolution, relaxation rate of the distribution function, specified by the relaxation time also affects the simulation result since it determines the location of the bounce back nodes on the interphase between the pore and the rock phases. Thus, the relaxation rate was also varied but for a fixed resolution (350^3 computational size) at Re $\sim$ 0, and the calculated permeability values were very similar for the different relaxation times, with 1.35% change between the maximum and minimum values. Therefore, for this domain with uniform geometry, the simulation results can be considered to be independent of relaxation time. As earlier mentioned in the Poiseuille flow analysis, $\lambda = 0.9$ will be used for further analysis. The maximum obtainable Re before the onset of compressibility error (maximum lattice velocity $\approx$ 0.057 *lu* at $Ma = 0.1$) for $\lambda = 0.9$ (lattice viscosity $\approx$ 0.1333 *lu*) is given by

$$Re_{max} = \frac{u_{lu_{max}} D_{p_{lu}}}{\nu_{lu}}; \qquad u_{lu_{max}} \approx 0.057 \tag{23}$$

From the aforementioned formula, $\mathrm{Re}_{\max} = 129$ for the BCC sphere pack at $N = 350$, while the maximum simulated Re in the domain in this work is 83. The permeability estimates obtained were compared with the Carman-Kozeny and Ergun formulas, respectively, as shown in the following

$$K = \begin{bmatrix} 11.7 & 0 & 0 \\ 0 & 11.7 & 0 \\ 0 & 0 & 11.7 \end{bmatrix} D \quad k_{CK} = 9.23\mathrm{D} \quad k_{Ergun} = 11.08\mathrm{D}$$

Diagonal elements of the permeability tensor obtained from simulation results compare well against the analytical estimates.

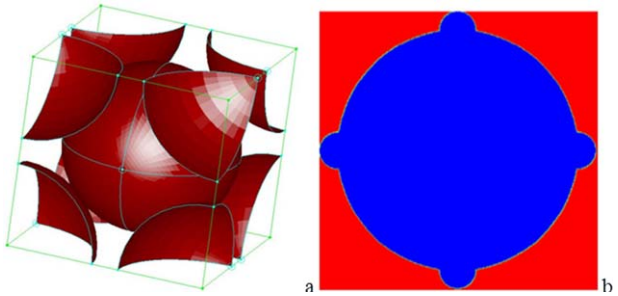

Figure 4. Sphere pack geometry and arrangement of roughness elements.

(a) Body centered cubic (BCC) sphere pack, and (b) 2-D representation of roughness on the regular BCC sphere pack. [Color figure can be viewed in the online issue, which is available at wileyonlinelibrary.com.]

To investigate in detail, the behavior of the permeability and average length of the flow-paths in the BCC sphere packing at 350^3 lattice size, the *y*-direction permeability and estimates of tortuosity obtained from Eqs. 17 and 18 are plotted as shown in Figure 6a. On the graph, permeability is constant up to Re = 4.0 beyond which it decreases as Re increases, due to contribution of inertia to high-flow regimes. Tortuosity also followed a similar trend as the permeability, with transition occurring at Re = 4.0. The region of constant permeability and tortuosity signifies the viscous dominated regime for which Darcy's law is valid. In addition, τ is the same as τ_1 at low Re, but less than τ_1 at high Re as fluid particles recirculate in the domain, in agreement with the earlier explanation. However, additional trend in the tortuosity plot is observed as the estimates only decreased till Re = 15.0 and Re = 30.0, respectively for τ and τ_1 and then increased in value beyond this Re for τ_1. Following are the tortuosity estimates for the BCC sphere packing at low Re

$$\tau = \tau_1 = \begin{bmatrix} 1.23 & 0 & 0 \\ 0 & 1.23 & 0 \\ 0 & 0 & 1.23 \end{bmatrix}$$

For a unit length of BCC cubic packing, the average length of all the flow paths through the domain is approximately 1.23 *L*, where *L* is the flow domain length.

To obtain the non-Darcy coefficient in the ***y***-direction, the inverse of k_y obtained for different Reynolds numbers were plotted against a pseudo-Reynolds number as shown in Figure 6b. In accordance with Eq. 20, a straight line graph is obtained with intercept equal to the intrinsic permeability, while beta factor was calculated from the slope. It is observed from the graph that, in addition to the region of slope equal to zero (Darcy's regime), two linear regimes are obtained which are here termed the Forchheimer, and post-Forchheimer regions, respectively. Transition from the Darcy

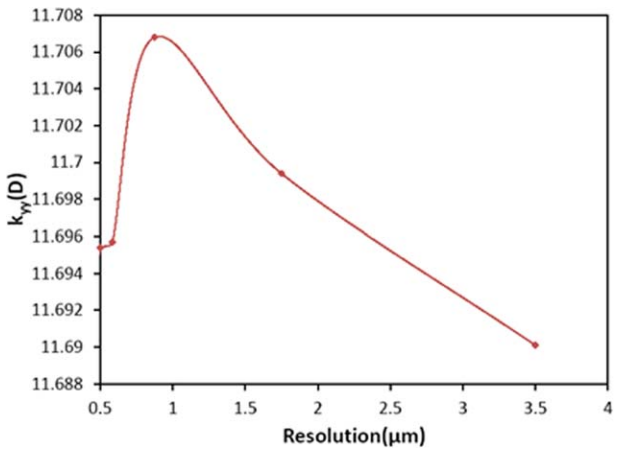

Figure 5. Variation of apparent permeability with resolution of BCC sphere.

Note the vertical axis scale for calculated permeability values (~11.69 ± 0.01D). [Color figure can be viewed in the online issue, which is available at wileyonlinelibrary.com.]

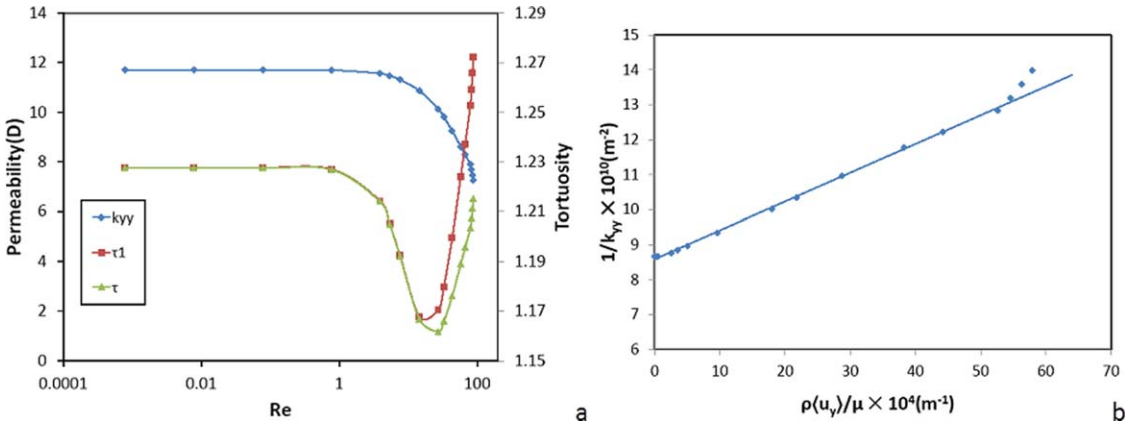

Figure 6. Inertial flow effects.

(a) Variation of apparent permeability (diamonds) and tortuosity values (squares, triangles) of BCC sphere with Reynolds number, and (b) inverse of apparent permeability vs. pseudo-Re. [Color figure can be viewed in the online issue, which is available at wileyonlinelibrary.com.]

to Forchheimer region occurs at pseudo-Re $\approx 2.6 \times 10^4$ m^{-1} (Re $\sim$ 4), while transition from Forchheimer to post-Forchheimer regime occurs at pseudo-Re $\approx 50.4 \times 10^4$ m^{-1} (Re $\sim$ 79). We postulate that the post-Forchheimer region is a result of flow separation occurring at high Reynolds number as seen in Figure 7d. From these linear sections for similar graphs for x, z-directions, respectively, the diagonal components of the non-Darcy coefficients tensor which are the same for all directions are obtained and presented below

$$\beta = \begin{cases} 0; Re < 4 \\ 7.5\times10^4 m^{-1}; 4 < Re < 79 \\ 2.3\times10^5 m^{-1}; 79 < Re \end{cases}$$

We reiterate that Darcy permeability is the intercept obtained by extending the plot of the first linear section to the y-axis and not the intercept of the second linear region, which would have produced a negative value. Off-diagonal components of β tensor were obtained as zero because of the periodicity of the domain. In addition, the Ergun estimate of $\beta =$ compares well with non-Darcy coefficient estimated for the linear regime at Re $>$ 79. The steady state velocity fields obtained from simulating flow in the BCC sphere pack at two different Re are shown in Figure 7a and 7b. In addition, flow streamlines are shown in Figures 7c and 7d for low and high Re, respectively and characteristic of inertial flows, eddies can be seen around the particles in the inset of Figure 7d, while the streamlines at the low Re are parallel to each other as shown in the inset of Figure 7c. These streamlines

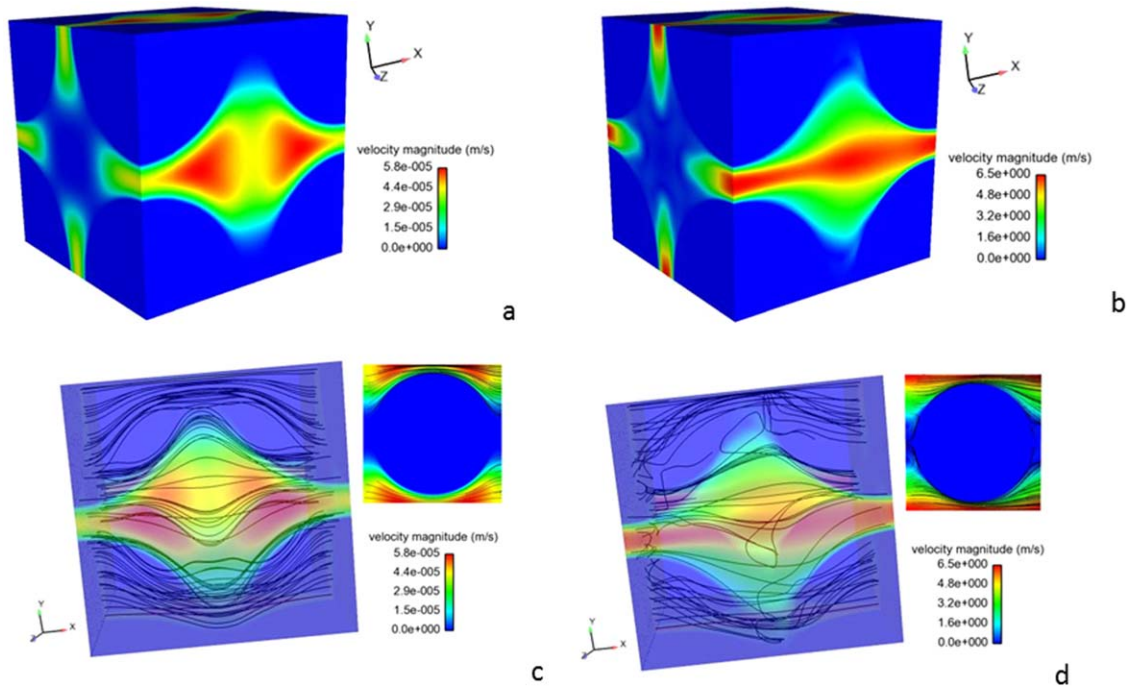

Figure 7. Flow field details in smooth sphere pack.

(a) Velocity field at Re $\approx$ 0 (max. velocity ~ 6×10-5m/s), (b) velocity field at Re = 85 (max. velocity ~ 6.5 m/s), (c) streamlines in BCC sphere domain at Re$\approx$0, and (d) streamlines in BCC sphere domain at Re = 85. [Color figure can be viewed in the online issue, which is available at wileyonlinelibrary.com.]

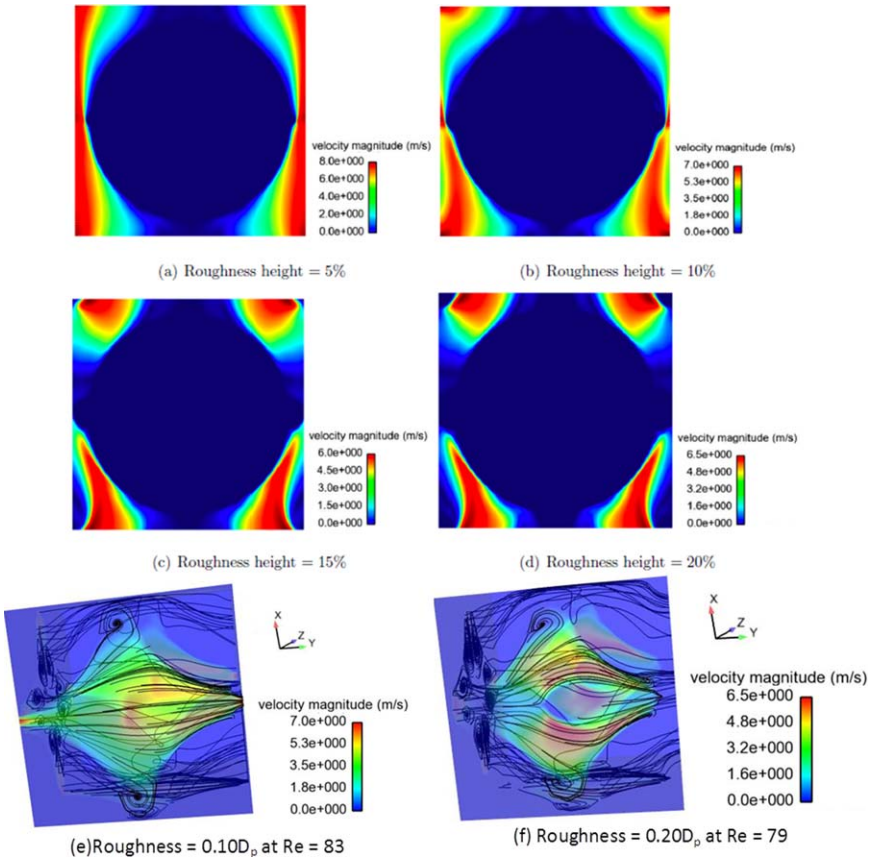

Figure 8. Flow field details in rough sphere packs.

(a-d) Velocity magnitude distribution for flow (from bottom to top) through the rough domains, flow streamlines though domain at (e) 10% roughness heights at Re = 83, and (f) 20% roughness height at Re = 79. [Color figure can be viewed in the online issue, which is available at wileyonlinelibrary.com.]

show the fluid flow direction through all percolation pathways in the domain.

Effect of grain roughness on macroscopic flow parameters

In the previous section, the macroscopic transport properties for the regularly arranged (BCC) sphere packs were obtained from LBM results at different flow conditions. In carrying out the simulation, the media were assumed to be composed of smooth spheres and this assumption was ideal to obtain results that are verifiable using analytical equations. On the other hand, in addition to the complex nature of the solid-pore interface, porous media in natural systems are characterized by rough interfaces that may impact significantly on the pore-scale flow behavior. Formation of these rough surfaces could be due to the result of deposition of clay and other minerals on the rock matrix, from partial dissolution of the rock matrix, or from fracturing or grain shearing arising from increased overburden pressure. In all of these conditions, the flow parameters will be different from similar size and configuration systems without roughness. Thus, it is important to quantify the effect of grain roughness on flow parameters and how much these calculated parameters deviate from the original systems. In this section, flow is simulated on a BCC arrangement of rough spheres with protrusions on the spheres acting as the surface roughness. The surface protrusions are modeled as depositions of hemispherical particles, placed on locations at which planes tangent to the surface of the sphere are parallel to the sides of the domain as shown in Figure 4b. Six of these protrusions are defined on each sphere and the height is expressed as a percentage of the diameter of the smooth sphere.

We simulated for four different roughness heights of 0.20, 0.15, 0.10, and 0.05 times the diameter of the sphere (D_p) and estimated the permeability, tortuosity and beta factor at these roughness conditions. Figure 8a–d shows the flow field on a 2-D slice of the rough spheres, delineating the magnitude of the protrusion as given by their heights. Comparing the streamlines of Figures 8e and 8f, it is seen that flow paths through the domain having a roughness height of $0.20D_p$ are more tortuous than those through the $0.05D_p$ roughness height domain. Similar relationship is expected when comparing a domain with larger roughness height to another with smaller roughness height.

This is reflected in the plot of tortuosity estimates at different Re for the domains, as shown in Figure 9b. At low Re, it is seen from the graph that τ and τ_1 are the same for each individual roughness domain but deviate from each other as Re increases, due to flow path separation, which is not considered in the definition of τ. Although the tortuosity trends are similar for flow through all the geometries, the value of the estimates increases with the roughness heights (Table 2). Thus, the average length of the flow paths through the domain with $0.20D_p$ roughness height is greater than those through $0.05D_p$ roughness domain. This behavior is further captured in the apparent permeability estimates for

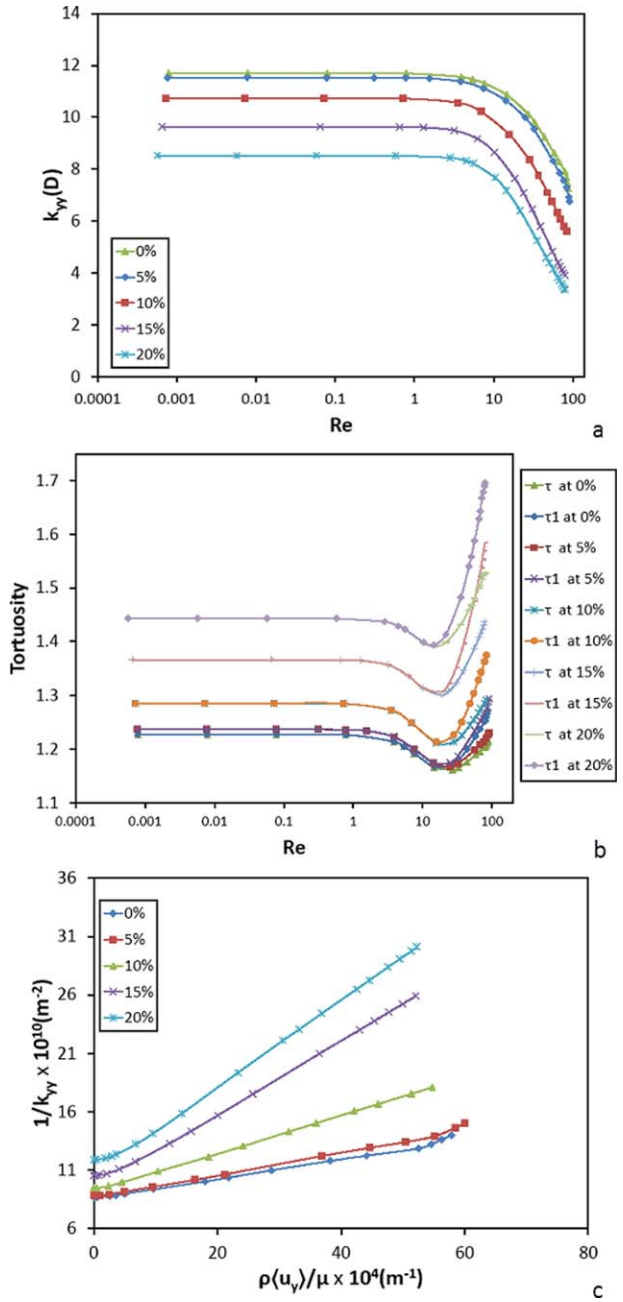

Figure 9. Effect of grain roughness and flow inertia.

(a) Permeability for different roughness domains at different Re (~ 0.001–100), (b) Tortuosity of different roughness (0.00–0.20) domains at different Re (~ 0.001–100), and (c) Inverse of apparent permeability vs. pseudo Re for different roughness heights (0.00–0.20). [Color figure can be viewed in the online issue, which is available at wileyonlinelibrary.com.]

the geometries at different Re as shown in Figure 9a. Again, the permeability trend for all the domains are the same and similar to that for the smooth sphere. However, the apparent permeability decreased as the roughness height increased. This finding is closely related to that for tortuosity since larger roughness heights signify greater resistance to flow, and, hence, a corresponding decrease in permeability. In addition, Figure 9a shows that flow deviation from the viscous dominated Darcy regime to the non-Darcy regime occurs within the same Re range (Re $\sim$ 4.0) for all the roughness heights and the smooth spheres domain. Finally, from the apparent permeability calculated at different Re from the LBM simulation results, the non-Darcy coefficient was obtained from the plot of the inverse of the apparent permeability vs. the pseudo-Re. The graph for all the domains is shown in Figure 9c, and it is seen that the plots become steeper as the roughness height increases leading to increase in β value. This result is attributed to the fact that flow path variability and curvature increases as the increasing height of rough obstructions impede flow through the porous media channels. Also, as fluid flows from inlet to outlet, more fluid recirculates behind the protruding roughness elements, as can be seen in Figure 8. Cumulative effect of these phenomena results in greater resistance to flow due to the larger roughness elements since a larger pressure drop will be required to achieve a given flow velocity. These effects reflect in increasing values of the beta factor for the domains. We also observe diminishing post-Forchheimer region in Figure 9 as roughness height increases. This may be attributed to the fact that at high Reynolds number, the effects of flow recirculation behind the protrusions outweigh the effect of flow separation that was observed for the case of smooth spheres.

Flow in an irregular pack of uniform spheres

Lastly, LBM is applied to the synchrotron microtomography 3-D image of a real porous medium that is comprised of irregularly arranged, uniform diameter (123 μm), smooth spheres as shown in Figure 10a. The tomographic image is discretized into 250 $\times$ 250 $\times$ 250 voxels with a resolution of 5.8 μm. Details of the CT beamline can be found at URL (http://tomo.camd.lsu.edu/). The simulation domain is the CT image itself since the computational nodes are defined in the center of the voxels. However, an additional layer of nodes was added to all sides of the domain to accommodate the boundary condition to be used. Thus the simulation domain is 252 $\times$ 252 $\times$ 252 nodes. Overall, only two extra layers were added in each direction as more blank cells will enhance the permeability of the medium.

Next, flow was simulated in a disordered sphere pack using the density gradient approach for pressure gradient with no flow boundaries on the sides of the sample and λ equal to 1.0. The results for tortuosity and permeability are presented below

Table 2. Effect of Roughness Height (Percent of Sphere Diameter) on the Calculated Porosity, Permeability, Tortuosity and Beta Factor of Rough BCC Sphere Pack.

Roughness	Φ	K (D)	$\tau \approx \tau_1$	$\beta \times 10^3$ (m^{-1})
0%	0.3206	11.70	1.227	75.5
5%	0.3203 (↓0.09%)	11.52 (↓1.48%)	1.237 (↑0.77%)	94.9 (↑25.72%)
10%	0.3184 (↓0.68%)	10.73 (↓8.22%)	1.286 (↑4.73%)	163.2 (↑116.26%)
15%	0.3132 (↓2.32%)	9.64 (↓17.60%)	1.365 (↑11.28%)	319.1 (↑322.75%)
20%	0.3039 (↓5.21%)	8.53 (↓27.05%)	1.443 (↑17.56%)	370.0 (↑390.21%)

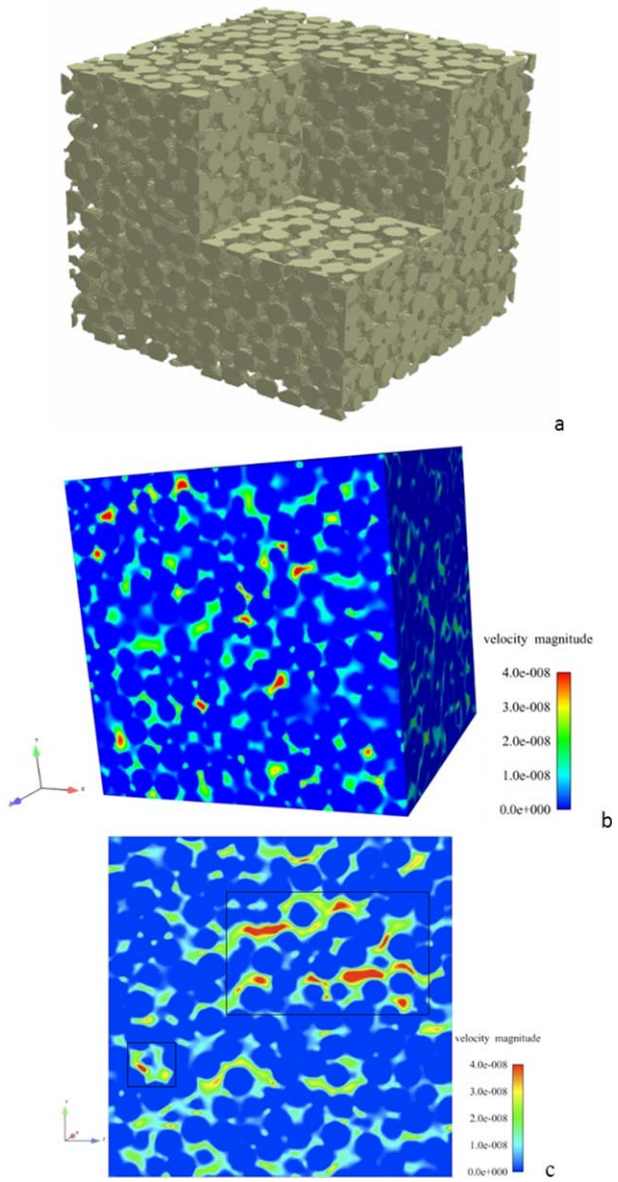

Figure 10. Flow details in imaged real porous media.

(a) CT imaged irregular pack of uniform spheres, (b) flow field in 3-D domain, and (c) flow field on 2-D slice at x mid-plane. [Color figure can be viewed in the online issue, which is available at wileyonlinelibrary.com.]

$$K = \begin{bmatrix} 16.4 & 0 & 0 \\ 0 & 16.57 & 0 \\ 0 & 0 & 15.02 \end{bmatrix} D \quad \tau = \begin{bmatrix} 1.5753 & 0 & 0 \\ 0 & 1.573 & 0 \\ 0 & 0 & 1.682 \end{bmatrix}$$

$$\tau_1 = \begin{bmatrix} 1.578 & 0 & 0 \\ 0 & 1.576 & 0 \\ 0 & 0 & 1.670 \end{bmatrix} \quad K_{CK} = 16.41 \text{ D} \quad \Phi = 0.40747$$

Off-diagonal components of the results presented previously are zeros since a no flow boundary condition is imposed in the direction other than that of the applied pressure gradient. The difference in values of the diagonal components of the tortuosity and permeability shows that the domain is not periodic, although the permeability values compare well with the Carman-Kozeny estimate (16.41 D). In addition, the tortuosity is greater than that for regular BCC arrangement since the spherical particles are randomly distributed and for this reason, increases the average length of path traveled by the fluid particles in the domain.

On the global scale of the sample, inertia dominated flow was not obtained since high-flow regimes could not be simulated. High-flow rate regimes require good resolution of sample pore spaces and for the random sphere pack, the resolution of 5.8 μm was not sufficient to resolve the pore spaces, especially the small ones. This is better understood from the perspective of maximum obtainable Reynolds number. For this computational domain, with $D_p = 21$ *lu* and applying Eq. 23, $\text{Re}_{\max} \sim 9.0$ which is close to the maximum simulated value of Re $\sim$ 6.0. A high Re flow can be simulated on this sample if the resolution is increased by a factor approximately equal to the amount by which Re $\sim$ 6.0 is increased. For very high Re values however, the required resolution level may be impractical to achieve given present imaging capabilities. On the other hand, the physical size of the sample can be reduced and then imaged at the same or higher resolution than 5.8 μm.

The velocity distribution obtained from the LBM simulations are shown in Figure 10b and 10c. From Figure 10b which shows velocity magnitude in the 3-D domain of the sample, for flow in the x-direction from left to right of the image, it is seen that flow velocity is generally low. However, isolated regions with high velocity, represented by hotter colors, are easily identified. These regions are further highlighted by the rectangular insets in the flow distribution on the 2-D slice of Figure 10c and they represent areas in the sample where local pore geometry was favorable to development of inertial flows. Thus, even though inertia dominated flow could not be simulated globally in the domain, inertial contributions can be identified locally in regions with small pore sizes (pore throats) and hence, high velocities as represented by the hot colors (Figure 10).

Discussion

Earlier attempts for beta factor prediction involved either less detailed models such as pore-network model[5] or stochastically generated 2-D pore spaces.[6] To authors' knowledge, the capability of LBM to simultaneously predict absolute permeability and beta factor has not been verified and validated in any systematic study in the open literature and thus, it is one of the original attempts to define 3-D canonical studies for inertial flows in porous media.

Simulation results confirmed the existence of the two regimes; viscous dominated regime characterized by constant permeability and inertia-dominated regime with decreasing permeability at increasing Reynolds number. This was further supported by the nature of the flow path observed in the visualized flow fields at these two conditions. At low Reynolds number characteristic of Darcy regime, the flow paths were parallel to each other and to the boundaries of the obstacles while at high Reynolds numbers in the non-Darcy regime, eddies were formed due to flow recirculation. Transition from Darcy to non-Darcy regime occurred within the range reported in literature for distribution of spheres (Re $\sim$ 1–10). In addition, the presence of roughness increased the flow path length of the smooth BCC arrangement and thus, increased the tortuosity and non-Darcy coefficients while decreasing the permeability since the domain became more resistant to flow as compared to the smooth sphere

arrangement. Systematic variation of roughness in an otherwise regular sphere pack results in a canonical problem to study effects of roughness on macroscopic flow parameters.

To this end, inertial flows in a realistic (image based) porous media for the Castlegate sandstone were also investigated by Chukwudozie et al.[35] Interplay between the image resolution and computational grid is expected to influence the prediction of macroscopic properties of such image-based porous media as it is likely that the computational domain contains under-resolved pore spaces.[36] A computational tool with verification and validation studies can now facilitate the advances in the pore scale inertial flow models using LBM.

Conclusion

Lattice Boltzmann method (LBM) is used to simulate flow in a computer generated three-dimensional BCC sphere packs of varying roughness and a real porous media obtained by CT imaging of a random sphere distribution. From the volume averaged simulation results, the media permeability, tortuosity and beta factor were calculated and compared with the Ergun and Kozeny-Carman estimates where available. Also, flow distributions obtained from the simulation were visualized to highlight the important flow paths and the velocity distribution in the porous medium. Our results showed good comparison for permeability and beta factor (non-Darcy coefficient) between simulation and Kozeny-Carman and Ergun estimates.

Acknowledgments

Authors are grateful to Exxon Mobil Upstream Research Co. for funding the project. We would like to thank Prof. Karsten Thompson (Petroleum Engineering) and Prof. Clint Willson (Civil and Environmental Engineering) for discussions and graciously providing the CT image file of the irregularly arranged sphere pack for LBM simulation. We also acknowledge the OpenLB group (www.lbmethod.org) for the open source code used for LBM simulations in this study. Finally, we acknowledge the LSU Center for Computation and Technology (CCT) and Louisiana Optical Network Initiative (LONI) for providing the high performance computing resources.

Notation

Symbols

β = beta factor
λ = relaxation parameter for the collision term in LBM
φ = porosity
τ = tortuosity

Letters

u = velocity
p = pressure
f = particle distribution function
Re = Reynolds number
K = permeability
D = Darcy or diameter (with subscript)

Subscripts

α = lattice velocity direction index
p = particle/grain

Unit conversion

1 D = $9.869233 \times 10-13$ m^2

Literature Cited

1. Dullien FAL. Porous Media - Fluid Transport and Pore Structure. Academic Press; 1979.
2. Whitaker S. The Forchheimer equation: A theoretical development. *Transp Porous Media*. 1996;25:27–61.
3. Whitaker S. Flow in porous media I: A theoretical derivation of Darcy's law. *Transp Porous Media*. 1986;1:3–25.
4. Ruth D, Ma H. On the derivation of the Forchheimer equation by means of volume averaging theorem. *Transp. Porous Media*. 1992;7: 255–264.
5. Balhoff MT, Wheeler MF. A predictive pore scale model for non-Darcy flow in anisotropic porous media. *SPE 110838*. 2007.
6. Newman M, Yin XL. Lattice Boltzmann simulation of non-Darcy flow in stochastically generated 2D porous media geometries. *SPE 146689*. 2011.
7. Chung TJ. Computational Fluid Dynamics. Cambridge University Press; 2002.
8. Chen S, Doolen GD. Lattice Boltzmann Method for fluid flows. *Annu Rev Fluid mech*. 1998;30:329–364.
9. Aidun CK, Clausen JR. Lattice-Boltzmann method for complex flows. *Annu Rev Fluid Mech*. 2010;42:439–72.
10. Sukop M, Thorne D. Lattice Boltzmann Modeling - An Introduction for Geoscientists and Engineers. New York: Springer; 2005.
11. Succi S, Foti E, Higuera F. Three-dimensional flow in complex geometries with the lattice Boltzmann method. *Europhys Let*. 1989;10: 433–438.
12. Ferreol B, Rothman DH. Lattice-Boltzmann simulations of flow through Fontainebleau porous media. *Transp Porous Media*. 1995; 20(1-2): 3–20.
13. Martys NS, Chen H. Simulation of multicomponent fluids in complex three-dimensional geometries by the lattice Boltzmann method. *Phys Rev E*. 1996;53:743–751.
14. Jin G, Patzek TW, Silin DB. Direct prediction of the absolute permeability of unconsolidated and consolidated reservoir rock. *SPE 90084*. 2004.
15. Sholokhova Y, Kim D, Lindquist WB. Network flow modeling via lattice-Boltzmann based channel conductance. *Adv Water Res*. 2009; 32:205–212.
16. Nabovati A, Sousa ACM. Fluid Flow simulation in random porous media at pore level using the lattice Boltzmann method. *J Eng Technol*. 2007;2:226–237.
17. Rahmati AR, Ashrafizaadeh M. A generalized Lattice Boltzmann Method for three-dimensional incompressible fluid flow simulation. *J Appl Fluid Mech*. 2009;2:71–95.
18. Pan C, Hilpert M, Miller CT. Lattice-Boltzmann simulation of two-phase flow in porous media. *Water Res Res*. 2004;40:W01501.
19. Kang Q, Lichtner PC, Janecky DR. Lattice Boltzmann method for reacting flows in porous media, *Adv Appl Math Mech*. 2010;2(5): 545–563. doi:10.4208/aamm.10-10S02.
20. Jeong N. Advanced study about the permeability for micro-porous structures using the Lattice Boltzmann method. *Transp Porous Media*. 2009.doi:10.1007/s11242-009-9400-7.
21. Jeong N, Choi DH, Lin CL. Prediction of Darcy-Forchheimer drag for micro-porous structures of complex geometry using the lattice Boltzmann method. *J Micromech. Microeng*. 2006;16:2240.
22. Inamuro T, Yoshino M, Ogino F. Lattice Boltzmann simulation of flows in a three-dimensional porous structure. *Int J Num Meth Fluids*. 1999;29:737–748.
23. Johns, ML, Sederman, AJ, Bramley, AS, Gladden, LF, Alexander, P. Local Transitions in Flow Phenomena through Packed Beds Identified by MRI. *AICHE J*. 2000;46:2151–2161.
24. Suekane T, Yokouchi Y, Hirai S. Inertial flow structures in a simple-packed bed of spheres. *AIChE J*. 2003;49:10–17.
25. Gunjal PR, Ranade VV, Chaudhari RV. Computational study of a single-phase flow in packed beds of spheres. *AIChE J*. 2005;51:365–378.
26. Robbins DJ, El-Bachir MS, Gladden LF, Cant RS, von Harbou E. CFD Modeling of Single-Phase Flow in a Packed Bed with MRI Validation. *AIChE J*. 2012. doi:10.1002/aic.13767.
27. Ben Clennell M. Tortuosity: a guide through the maze. Geological Society, London, Special Publications. 1997;122:299–344.
28. Huang H, Ayoub J. Applicability of the Forchheimer equation for non-Darcy flow in porous media. *SPE 102715*. 2006.
29. Zeng Z, Grigg R. A criterion for non-Darcy flow in porous media. *Transp. Porous Media*. 2006;63:57–69.

30. Barree RD, Conway MW. Beyond beta factors: A complete model for Darcy, Forchheimer, and Trans-Forchheimer flow in porous media. *SPE 89325*. 2004.
31. Chen S, Martinez D. On boundary conditions in the lattice Boltzmann methods. *Phys Fluids*. 1996:8(9).
32. Zou Q, He X. On pressure and velocity boundary conditions for the lattice Boltzmann BGK model. *Phys Fluids*. 1997;9: 1591–1598.
33. Mei R. Shyy W, Yu D, Luo L.-S. Lattice Boltzmann method for 3-D flows with curved boundary. *J Comput Phys*. 2000;161:680–699.
34. Jonas L. OpenLB user guide. Release 0.4. 2008.
35. Chukwudozie CP, Tyagi M, Sears SO, White CD. Prediction of non-darcy coefficients for inertial flows through the Castlegate sandstone using image-based modeling. *Transp Porous Media*. 2012.doi: 10.1007/s11242-012-0062-5.
36. Takbiri-Borujeni A, Lane N, Thompson K, Tyagi M. Effects of image resolution and numerical resolution on computed permeability of consolidated packing using LB and FEM pore-scale simulations Comput Fluids. 2013.http://dx.doi.org/10.1016/j.compfluid.2013.05.019.

Manuscript received July 3, 2012; revision received July 17, 2013, and final revision received Sept. 10, 2013.